THE JOURNAL OF PHYSICAL CHEMISTRY B
A JOURNAL OF THE AMERICAN CHEMICAL SOCIETY

pubs.acs.org/JPCB

Article

Effects of Organic Surface Contamination on the Mass Accommodation Coefficient of Water: A Molecular Dynamics Study

Jordan Hartfield, Eric Bird, and Zhi Liang*

Cite This: J. Phys. Chem. B 2024, 128, 585−595

Read Online

ACCESS | Metrics & More | Article Recommendations | Supporting Information

ABSTRACT: The mass accommodation coefficient (MAC), a parameter that quantifies the possibility of a phase change to occur at a liquid−vapor interface, can strongly affect the evaporation and condensation rates at a liquid surface. Due to the various challenges in experimental determination of the MAC, molecular dynamics (MD) simulations have been widely used to study the MAC on liquid surfaces with no impurities or contaminations. However, experimental studies show that airborne hydrocarbons from various sources can adsorb on liquid surfaces and alter the liquid surface properties. In this work, therefore, we study the effects of organic surface contamination, which is immiscible with water, on the MAC of water by equilibrium and nonequilibrium MD simulations. The equilibrium MD simulation results show that the MAC decreases almost linearly with increasing surface coverage of the organic contaminants. With the MAC determined from EMD simulations, the nonequilibrium MD simulation results show that the Schrage equation, which has been proven to be accurate in predicting the evaporation/condensation rates on clean liquid surfaces, is also accurate in predicting the condensation rate at contaminated water surfaces. The key assumption about the molecular velocity distribution in the Schrage analysis is still valid for condensing vapor molecules near contaminated water surfaces. We also find that under nonequilibrium conditions the adsorption of the water vapor molecules on the organic surface results in an adsorption vapor flux near the contaminated water surface. When the water surface is almost fully covered by the model organic contaminants, the adsorption flux dominates over the water condensation flux and leads to a false prediction of the MAC from the Schrage equation.

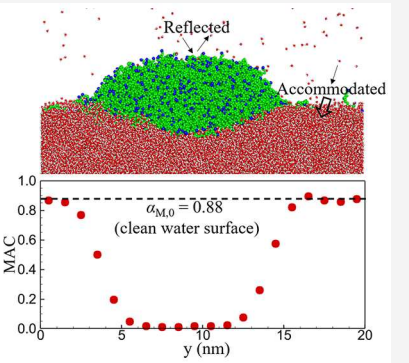

1. INTRODUCTION

Water evaporation and condensation play an important role in many environmental processes such as moisture transfer through clothing,[1,2] soil water evaporation and global warming,[3,4] and engineering applications such as evaporative cooling of electronic devices,[5] water desalination,[6] and medical therapy.[7] A fundamental understanding of the transport phenomena at an evaporating/condensing liquid surface requires treatment from the kinetic theory of gases (KTG).[8−11] Two relationships that have been widely used in the past decades to model evaporation and condensation processes are the Hertz−Knudsen (HK) relationships[8−10] and the Schrage relationships.[11,12] Both relationships were derived based on the KTG and provide an expression that correlates the evaporation/condensation flux with the temperature and density of fluid near a liquid−vapor interface and the mass accommodation coefficient (MAC).

When a vapor molecule strikes its own liquid phase, two things can happen: (i) the vapor molecule is accommodated to the liquid phase; (ii) the vapor molecule is reflected by the liquid surface, and no phase change occurs. The MAC is defined as the fraction of vapor molecules that strike a liquid−vapor interface and are accommodated in the liquid phase. Hence, the MAC quantifies the possibility of a phase change to occur for each collision between a vapor molecule and the liquid surface. Accurate measurement of the MAC by experiment is currently very challenging.[13] As a result, the validity of the HK and Schrage relationships in the prediction of evaporation and condensation rates has never been truly verified by experiment. One way to mitigate the experimental challenges in the MAC measurement is to use molecular dynamics (MD) simulations. A big advantage of MD modeling is that it can track the trajectories of each vapor molecule near the liquid−vapor interface. Hence, it can easily count the number of incident vapor molecules that are accommodated to the liquid phase or reflected by the liquid surface. MD simulations have been successfully used to determine the MAC of a variety of fluids including monatomic fluids,[14−19] polymers,[20−24] and water.[25−30]

Although the MAC of water has been extensively studied by MD simulations, all of the previous MD studies in the literature focused on the MAC at clean water surfaces.

Received: October 19, 2023
Revised: December 6, 2023
Accepted: December 11, 2023
Published: January 4, 2024

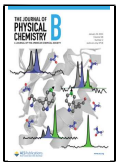

https://doi.org/10.1021/acs.jpcb.3c06939
J. Phys. Chem. B 2024, 128, 585−595

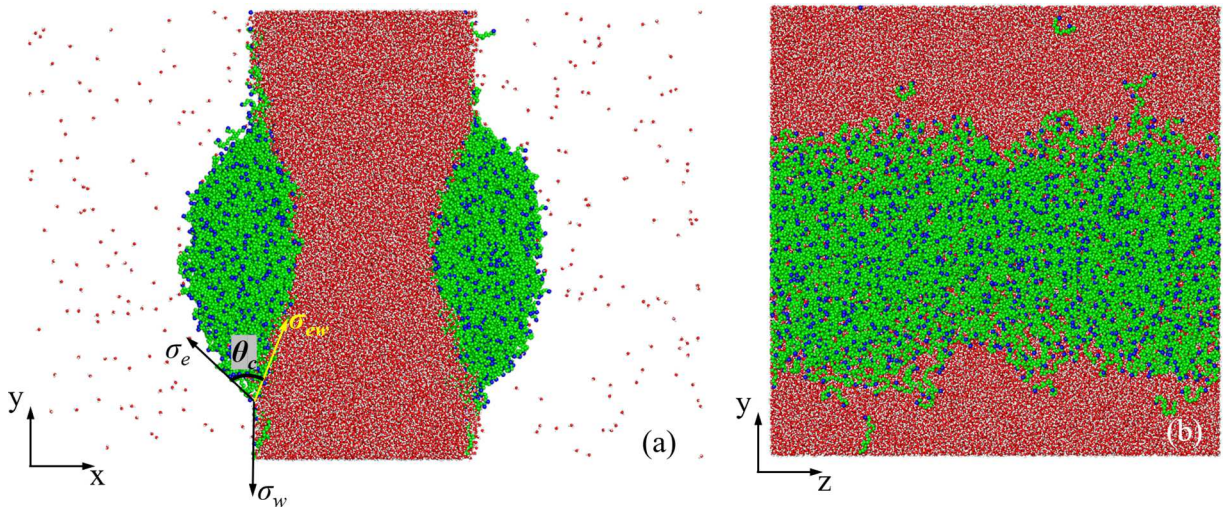

Figure 1. (a) $x-y$ view and (b) $y-z$ view of a snapshot of the EMD model system containing 2100 eicosane molecules and 95,700 water molecules after equilibration at a temperature of 400 K.

However, recent experimental studies show that airborne hydrocarbons, which are mainly generated by production, transport, and incomplete combustion of oil,[31] can be easily adsorbed by various types of solid and liquid surfaces.[32−36] It was shown that, within 24 h of exposure to the air, the accumulation of hydrocarbon contaminants to a surface can significantly alter surface properties such as wettability and critical heat flux of solid surfaces[32−34] and surface tension of water.[35,36] Hence, it is reasonable to expect that the hydrocarbon contamination on water surfaces will also affect the MAC and the evaporation and condensation rates of water. It was reported in numerous experimental studies that the MAC values measured in experiments with stagnant water surfaces are significantly lower than those with renewing water surfaces.[37,38] The general explanation of the discrepancies in the measured MAC values is that the accumulation of contaminants on stagnant water surfaces impedes the evaporation/condensation processes, leading to a much smaller MAC. However, this explanation has not been verified by experiment because it is difficult to know when contaminations are present, what type of contaminants are on water surfaces, and the surface coverage of contaminants in the experimental system.[13]

In this work, we carry out MD simulations to study the effects of organic surface contaminants on the MAC of water. The recent experimental study shows that the typical airborne hydrocarbon contamination from laboratory atmospheres consists of *n*-alkanes with molecular weight ranging predominantly from C_{15} to C_{22}.[32] In our MD model, therefore, we choose *n*-eicosane ($C_{20}H_{42}$), a representative hydrocarbon contamination in laboratory atmospheres, as the organic contaminant on the model water surfaces and investigate how the water MAC and condensation rate depend on the surface coverage of the model organic contaminant.

2. THEORY

In this work, we use both equilibrium MD (EMD) and nonequilibrium (NEMD) simulations to determine the MAC of water on contaminated water surfaces. In the EMD model, such as that shown in Figure 1, we directly count the number of vapor molecules incident on the contaminated water surface (N_{inc}) and the number of incident vapor molecules that are accommodated to the liquid water (N_{acc}) and determine the MAC (α_M) directly from its definition

$$\alpha_M = N_{acc}/N_{inc} \tag{1}$$

To investigate if the MACs determined from EMD simulations are consistent with those determined under nonequilibrium conditions, i.e., when net evaporation or condensation of water occurs, we also carry out NEMD simulations (see, e.g., Figure 2) of quasi-steady-state evaporation and condensation at the model water surface and determine α_M from the Schrage equation,[11−13]

$$J = \alpha_M \sqrt{\frac{R}{2\pi M}} (\rho_g(T_L)\sqrt{T_L} - \Gamma(v_R)\rho_v\sqrt{T_v}) \tag{2}$$

The Schrage equation predicts the evaporation/condensation flux J across a liquid−vapor interface at a temperature of T_L when the temperature and density of vapor near the liquid surface are T_v and ρ_v, respectively. In the Schrage equation, R is the universal gas constant, M is the molar mass of vapor molecules, and $\rho_g(T_L)$ is the saturated vapor density at T_L. If J is greater than 0, then net evaporation occurs. If J is less than 0, then net condensation occurs. The key assumption made in the derivation of the Schrage equation is that the velocity distribution (VD) of vapor molecules near an evaporating/condensing liquid−vapor surface follows the shifted Maxwell VD[11]

$$f(v_x) = \sqrt{\frac{M}{2\pi RT_v}} e^{-M(v_x - v_{v,0})^2/2RT_v} \tag{3}$$

where v_x is the molecular velocity component along the evaporation direction and $v_{v,0}$ is the macroscopic velocity of vapor near the liquid−vapor interface. When net evaporation occurs, $v_{v,0}$ is greater than 0. When net condensation occurs, $v_{v,0}$ is less than 0. In the Schrage equation, i.e., eq 2, the effects of macroscopic vapor motion are taken into account by the function $\Gamma(v_R)$, which is given by

$$\Gamma(v_R) = e^{-v_R^2} - v_R\sqrt{\pi}[1 - \mathrm{erf}(v_R)] \tag{4}$$

where v_R is the ratio of the macroscopic speed of vapor, $v_{v,0}$, to the most probable thermal speed of vapor molecules

https://doi.org/10.1021/acs.jpcb.3c06939
J. Phys. Chem. B 2024, 128, 585−595

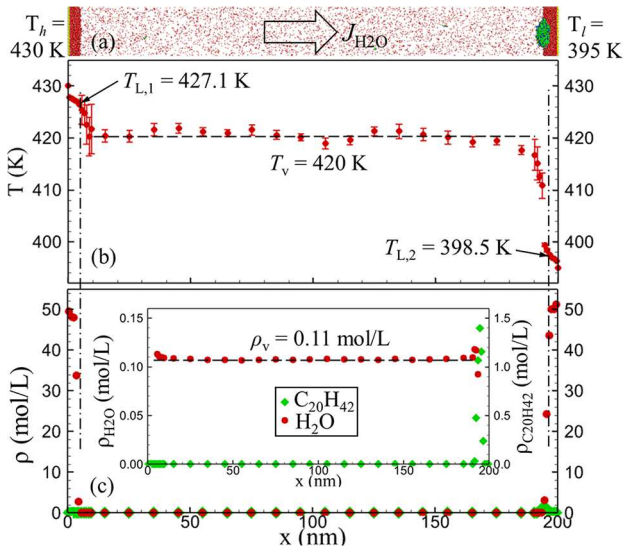

Figure 2. (a) A snapshot of the model system during NEMD simulation with T_h = 430 K, T_l = 395 K, and 54% surface coverage of organic contaminant on the condensing liquid surface. The yellow, red, white, blue, and green dots in the snapshot represent Au, O, and H atoms and CH_3 and CH_2 pseudoatoms, respectively (same in other figures). Steady-state (b) temperature and (c) density profiles in the model system. The inset in (c) shows the density profile in the gas region. The horizontal dashed lines in (b) and (c) indicate the average temperature and density in the gas region, respectively. The vertical dash-dot lines indicate the location of the liquid water surfaces.

$$v_R = \frac{v_{v,0}}{\sqrt{2RT_v/M}} \tag{5}$$

As shown in Figure 2, the NEMD simulation will allow us to determine the fluid temperature (T_L and T_v) and density ($\rho_g(T_L)$ and ρ_v) in the Schrage equation as well as the molar flux (J) and macroscopic velocity ($v_{v,0}$) of vapor near the liquid−vapor interface with high fidelity. Using these NEMD simulation results in the Schrage equation, therefore, we can find the MAC (α_M) at evaporating and condensing water surfaces. The Schrage equation was also used in the recent experimental work to estimate the MAC on water surfaces during a steady-state evaporation process.[39] Our recent MD studies show that the Schrage equation is accurate in the prediction of evaporation and condensing rates at clean liquid surfaces.[17−19,24,27,40] Since the VD of evaporating/condensing vapor molecules is an important indicator of the validity of the Schrage equation, we will also use MD simulations to directly measure the VD of condensing vapor molecules near a contaminated water surface to investigate if the key assumption of the shifted Maxwell VD, i.e., eq 3, in the Schrage analysis is still valid for water vapor near a condensing water surface with organic contamination.

3. MOLECULAR DYNAMICS SIMULATIONS

3.1. The MD Model System. We used both EMD and NEMD simulations to determine the MAC at a contaminated water surface. In the EMD model, we place a liquid slab consisting of 95,700 H_2O molecules in the middle of a simulation box, which has a length of 30 nm in the x direction and 20 nm in the y and z directions as shown in Figure 1. On each of the two liquid water surfaces, we initially place a liquid n-eicosane ($C_{20}H_{42}$) semicylinder. As shown in Table 1, the total number of eicosane molecules in the EMD model varies from 0 to 4564 to gradually increase the surface coverage of the organic contaminant on the model water surface. The simulation box size is fixed during the EMD simulation, and periodic boundary conditions (PBCs) are applied in all three directions. We carry out EMD simulations at a constant temperature of 400 K because at lower temperatures the number of water vapor molecules in the model system will be too small, leading to poor statistics of the EMD simulation results for the MAC.

In the NEMD model, the model water and eicosane fluid system is confined by two solid Au plates, as shown in Figure 2. Each Au plate is formed by a three-layered FCC (100) plane of solid Au with a cross-sectional area of 20 nm by 20 nm. The separation between the two inner solid Au surfaces is 200 nm. On each of the two inner surfaces, we place a thin liquid water film. The initial thickness of the film on each of the two solid surfaces is approximately 4.5 nm such that the liquid layers are thick enough to avoid effects of disjoining pressure on the equilibrium properties of the model water.[25] As shown in Figure 2(a), the left water surface in the NEMD model is a clean surface, while the right water surface contains organic contaminants with a surface coverage the same as that in each case of the EMD simulations shown in Table 1. In NEMD simulations, PBCs are applied in the y and z directions, and atoms in the outermost Au layers are fixed. The fluid in the region from x = 10 to 190 nm is always in a gaseous state in NEMD simulations. Therefore, we define this region as the gas region of the NEMD model system.

In NEMD simulations, the left and right Au plates are maintained at a temperature of 430 and 395 K, respectively, by velocity rescaling at each time step. This leads to evaporation of liquid water on the left clean water surface and condensation of water vapor on the right contaminated water surface as shown in Figure 2(a). We set the heat source and heat sink

Table 1. MD Simulation Results of Surface Coverage of Organic Contaminants, Contact Angle of Organic Contaminants on the Model Water Surface, the MAC on Contaminated Water Surfaces, and the Interfacial Thermal Conductance Determined from eq 10 as a Function of the Number of $C_{20}H_{42}$ Molecules in the EMD Model

Case no.	No. of $C_{20}H_{42}$ molecules	Surface coverage (%)	Contact angle (deg)	MAC		G_{lv} (MW/m^2·K)
				EMD	NEMD	
1	0	0		0.88 ± 0.01	0.90 ± 0.01	25.4 ± 1.8
2	760	25.3 ± 1.1	77 ± 6	0.66 ± 0.02	0.69 ± 0.02	17.7 ± 1.1
3	1278	42.0 ± 0.8	77 ± 5	0.53 ± 0.01	0.56 ± 0.01	15.4 ± 0.9
4	2100	54.3 ± 0.6	82 ± 2	0.43 ± 0.01	0.43 ± 0.01	10.2 ± 0.5
5	2984	65.8 ± 0.9	80 ± 3	0.32 ± 0.01	0.33 ± 0.02	7.3 ± 0.3
6	4564	98.2 ± 0.1		0.01 ± 0.01	0.07 ± 0.01	3.6 ± 0.3

https://doi.org/10.1021/acs.jpcb.3c06939
J. Phys. Chem. B 2024, 128, 585−595

temperatures to 430 and 395 K so that the temperature at the contaminated water surface during quasi-steady-state evaporation and condensation is always close to 400 K, i.e., the temperature used in the EMD simulation. In this case, we can compare the MAC determined from EMD and NEMD simulations at the same temperature and with the same surface coverage of the organic contaminants.

3.2. The Molecular Interaction Potential Model. In both EMD and NEMD simulations, we use a rigid extended simple point charge (SPC/E) model[41] to describe the intermolecular potential of water molecules. The Coulombic interactions in the SPC/E potential are treated by the Wolf summation[42] with a damping factor of 0.15 $Å^{-1}$ and a cutoff distance of 9.0 Å. The Wolf summation technique has been shown to produce reasonable saturated densities for SPC/E water.[43] We have successfully used the SPC/E model along with the Wolf summation technique for MD simulations of steady-state evaporation and condensation of water in our previous work.[27]

To model the intra- and intermolecular interactions of eicosane molecules, we use the united atom (UA) model proposed by Nath et al.[44] The UA model treats the hydrocarbon groups as pseudoatoms, i.e., single interaction sites. For bonded interactions within an eicosane molecule, the two-body bond stretching, the three-body bond bending, and the four-body torsion are modeled by the Khare et al. potential,[45,46] the van der Ploeg and Berendsen potential,[47] and the Jorgensen potential,[48] respectively. The nonbonded interactions between any two pseudoatoms that belong to the same molecule but are separated by more than three bonds are modeled by the Lennard-Jones (LJ) potential with parameters proposed by Smit et al.[49] The Smit et al. LJ potential is also used to model the interactions between pseudoatoms belonging to different molecules. The Lorentz−Berthelot (LB) mixing rule[50] is employed to determine the LJ parameters for interactions between CH_3 and CH_2 pseudoatoms. The cutoff distance for all LJ interactions between pseudoatoms is 13.8 Å.[44,49] We have successfully used the UA potential model for MD simulations of steady-state evaporation and condensation of *n*-dodecane in our previous work.[24]

For Au−Au interactions, we use the embedded-atom-method (EAM) potential.[51] The nonbonded interactions between Au and eicosane molecules and between Au and H_2O molecules are also described by the LJ potential with parameters taken from the universal force field (UFF)[52] and calculated by the LB mixing rule. The cutoff distance for the LJ interactions between Au and eicosane molecules and between Au and H_2O molecules is 13.8 and 9 Å, respectively. The LJ potential is also used for interactions between water and eicosane molecules. The LJ potential parameters determine the eicosane−water interfacial tension (σ_{ew}) as well as the contact angle (θ_c) and spreading coefficient (S) of eicosane on the model water surface. The relationship between the contact angle and the surface tension is given by[53]

$$\cos\theta_c = (\sigma_w^2 - \sigma_e^2 - \sigma_{ew}^2)/2\sigma_e\sigma_{ew} \quad (6)$$

where σ_w and σ_e denote the surface tension of water and eicosane, respectively. The spreading coefficient is defined as[53]

$$S = \sigma_w - (\sigma_e + \sigma_{ew}) \quad (7)$$

The spreading coefficient determines the eicosane−water wetting behavior, and thus the surface coverage of a given volume of eicosane on the water surface. It was shown in the recent MD study[54] that, for water modeled by the SPC/E model and alkanes modeled by the UA model, using the LJ potential parameters ε_{LJ} = 0.65 kJ/mol and σ_{LJ} = 3.6 Å for interactions between the O atom in water and the pseudoatoms in *n*-alkanes results in spreading coefficients agreeing well with experimental values. Therefore, we adopt these LJ potential parameters with a cutoff distance of 13.8 Å in our MD model with the hope of achieving more realistic predictions of wetting of water by eicosane.

3.3. Simulation Details. In MD simulations, a velocity Verlet algorithm is used to integrate the equations of translational motions.[55] A leapfrog algorithm for quaternions developed by Omelyan[56] is used for integration of the equations of rotational motions of water molecules. A time step size of 1 fs is used in all MD simulations.

In EMD simulations, the model system is first equilibrated at a temperature of 400 K for 2 ns using the Berendsen thermostat.[57] After 2 ns of equilibration, the geometry of eicosane on the water surface and the vapor density become stable. The thermostat is then applied for another 2 ns, and the model system is evenly divided into 120 bins in the x direction with a bin size of 0.25 nm to determine the distribution of fluid properties and the MAC from the EMD simulation as shown in Figure 3. In the 2 ns production run, we output the positions of each atom in the model system every 100 ps which results in 20 snapshots of the model fluids. Each $x-y$ projection of the snapshot is used to measure the contact angle (θ_c) of eicosane

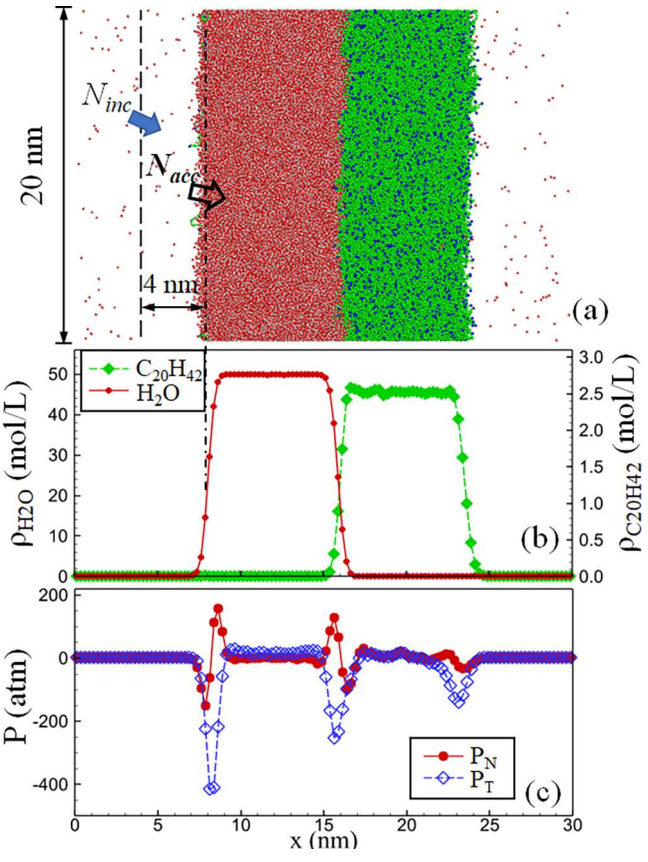

Figure 3. (a) A snapshot of the model system containing a 7.5 nm water layer in contact with a 7.5 nm eicosane layer in thermal equilibrium at a temperature of 400 K. (b) The density profile and (c) the distribution of normal pressure (P_N) and tangential pressure (P_T) in the model system.

https://doi.org/10.1021/acs.jpcb.3c06939
J. Phys. Chem. B 2024, 128, 585−595

on the model water surface as shown in Figure 1(a). Each $y-z$ projection of the snapshot is used to determine the surface coverage (sc) of eicosane on the water surface as shown in Figure 1(b). The sc is calculated using the ratio of green (represents CH_2 pseudoatoms) and blue (represents CH_3 pseudoatoms) pixels to all pixels in the snapshot. The uncertainties in θ_c and sc in each simulation case are determined by analyses of the 20 snapshots. The details of how each snapshot is processed to determine θ_c and sc are described in the Supporting Information.

In NEMD simulations, each heat source-sink simulation run is first carried out for 5 ns to allow the system to reach quasi-steady-state evaporation and condensation, which means the evaporation and condensation flux becomes essentially time-independent after 5 ns. Subsequently, the NEMD simulation is carried out for an additional 2 ns for data collection and averaging. We consider the simulated process as a quasi-steady-state evaporation and condensation process because the two liquid−vapor interfaces move at a speed below 0.2 m/s and during the 2 ns data collection period the interfaces only displace by less than 4 Å for all simulation cases shown in Table 1. To calculate the steady-state profiles of fluid properties as shown in Figure 2, we evenly divide the fluid region less than 10 nm from each of the two solid surfaces into ten bins. The 1 nm bin width in this region allows us to find the location and temperature of the liquid surface with precision. In the 180 nm-long gas region, we evenly divided the region into 18 bins. The 10 nm bin width allows us to obtain good statistics of vapor properties that will be used in the Schrage equation to determine the MAC. The contribution from the vapor macroscopic velocity is subtracted in the calculation of temperature in each bin. To further improve the accuracy of the simulation results, four independent runs are performed in each case of NEMD simulations. The uncertainties in the NEMD simulation results are determined by analyses of these independent runs.

4. RESULTS

4.1. Saturated Density and Wetting Behavior of Model Fluids. To determine the saturated density and wetting behavior of the model fluids, we first carry out an EMD simulation in a simulation box containing a 7.5 nm-thick liquid water layer in contact with a 7.5 nm-thick liquid eicosane layer, as shown in Figure 3(a). After 2 ns of equilibration at a temperature of 400 K, the liquid water and eicosane are in equilibrium with their saturated vapor in the simulation box. From the density profile shown in Figure 3(b), we find that the saturated liquid water and liquid eicosane density are 49.9 ± 0.1 and 2.52 ± 0.03 mol/L, respectively, which are in reasonable agreement with the experimental data of 52.0 mol/L (water[58]) and 2.54 mol/L (eicosane[59]). The saturated water vapor density is 0.058 ± 0.002 mol/L which is the same as that found in our previous work on a pure water system.[27] The saturated eicosane vapor density at 400 K is found slightly below 10^{-4} mol/L. Such a low density is consistent with the low saturated eicosane vapor pressure ($\sim 10^2$ Pa) found in experiment at 400 K.[59]

To obtain the prediction of the eicosane−water wetting behavior, we use the EMD simulation to calculate the surface tension of the model fluids. It is shown in Figure 3(c) that the normal pressure (P_N) is almost the same as the tangential pressure (P_T) in the bulk liquid phase and bulk vapor phase of the model system but higher than P_T in the interface regions due to the surface tension. Using P_N and P_T from the EMD simulation, we calculate the surface tension from its mechanical definition,[60,61]

$$\sigma = \int_{x_1}^{x_2} [P_N(x) - P_T(x)]\, dx \tag{8}$$

Based on the pressure tensor profile in Figure 3(c), the integral in eq 8 from $x_1 = 0$ to $x_2 = 12$ nm, from $x_1 = 12$ to $x_2 = 19$ nm, and from $x_1 = 19$ to $x_2 = 30$ nm predicts $\sigma_w = 0.031$ N/m (water), $\sigma_{ew} = 0.024$ N/m (water−eicosane), and $\sigma_e = 0.016$ N/m (eicosane), respectively. Substituting the calculated surface tensions into eqs 6 and 7, we obtain the spreading coefficient $S = -0.009$ N/m and contact angle $\theta_c \approx 80°$. The negative spreading coefficient indicates partial wetting of the model water by eicosane. To corroborate the theoretical prediction of $\theta_c \approx 80°$, we directly measure the θ_c of eicosane on the model water surface obtained from EMD simulations. In the representative case (i.e., Case #4 in Table 1) shown in Figure 1, the measured θ_c is 82 ± 2° when the sc of eicosane on the model water surface is 54.3 ± 0.6%. We further vary the eicosane sc from 25% to 66% in the EMD model. As shown in Table 1, the measured θ_c in all simulation cases is consistent with the theoretical prediction from eq 6. We also found that the saturated water vapor density (ρ_g) is not affected by eicosane surface contamination in all simulation cases. Hence, we will use ρ_g obtained at the clean water surface[27] for the subsequent NEMD determination of MAC in Section 4.3. When the number of eicosane molecules in the EMD model increases to 4564 (Case #6 in Table 1), we observe the liquid water is almost fully covered by a 3.5 nm-thick eicosane layer due to the PBCs applied in the simulation. In this case, it takes 12 ns for the vapor phase to eventually reach saturated density.

4.2. EMD Determination of MAC. In EMD simulations, we determined the MAC from its definition, i.e., eq 1. To count the number of water vapor molecules that strike the liquid−vapor interface, we set an imaginary plane 4 nm from the liquid−vapor interface, as shown in Figure 3(a). Four nm is only 1/10 of the mean free path of the saturated water vapor molecules at a temperature of 400 K.[27] Hence, the collision between the incident vapor molecule and other vapor molecules near the liquid−vapor interface is very rare compared with the collision with the interface. The position of the liquid−vapor interface is defined at the plane where the water density is equal to half the saturated liquid water density as shown in Figure 3. We define water vapor molecules that cross the imaginary plane and move toward the interface as incident molecules. Once an incident vapor molecule crosses the liquid−vapor interface, we count it as an incident molecule that is accommodated in the liquid phase. The two-plane method has been widely used in MD simulations to determine the MAC.[15−19,24,25,27] By counting the fraction of incident vapor molecules that are accommodated to the liquid phase in the EMD simulation, we find the MAC on a clean water surface at a temperature of 400 K is 0.88 ± 0.01. This value is consistent with the previous MD studies[25−27] on the MAC of SPC/E water, which all show the MAC on a clean water surface is around 0.9 at T = 400 K. Furthermore, Figure 4 shows the calculated MAC on a clean water surface ($\alpha_{M,0}$) decreases with increasing temperature, which is also consistent with that found in the previous MD studies.[25−27] We also find that precise definition of the liquid−vapor interface position is not that consequential to the calculation of the MAC. As long as the liquid−vapor interface is defined at a position between

https://doi.org/10.1021/acs.jpcb.3c06939
J. Phys. Chem. B 2024, 128, 585−595

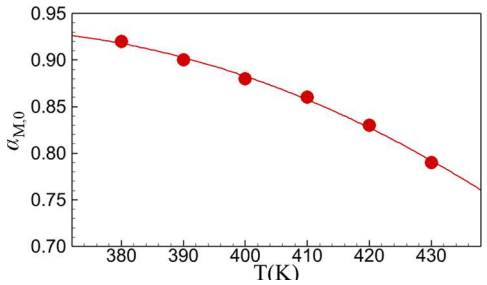

Figure 4. MAC on the clean water surface as a function of temperature obtained from EMD simulations. The solid line is the 2nd order polynomial fit to the MD data.

the plane where the water density is 10% of the liquid density and the plane where the water density is 90% of the liquid density, the deviation of the calculated MAC is less than 2%. To be consistent in this work, we used the half liquid density criterion to define the liquid−vapor interface in all simulation cases.

When the water surface is partially covered by the organic contaminants, the incident water vapor molecules can be directly reflected by or be adsorbed and then desorbed by the organic surface contaminants. Accordingly, a smaller fraction of incident molecules will be accommodated to the liquid water phase. For the representative case with a contaminant sc of 54% shown in Figure 1, the EMD simulation shows $\alpha_M = 0.43 \pm 0.01$. To have a better understanding of this result, we evenly divide the contaminated liquid surface into 20 bins in the y direction as shown in Figure 5 and determine the local MAC in

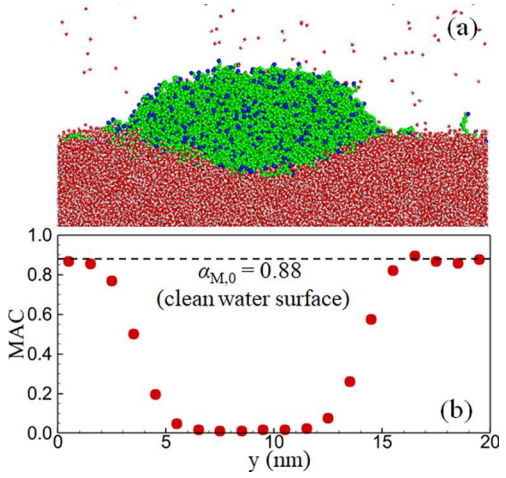

Figure 5. (a) A snapshot of the water surface with 54% surface coverage of the organic contaminant. (b) The MAC in different regions of the contaminated surface obtained from the EMD simulation. The horizontal dashed line indicates the MAC on the clean water surface.

each bin from the EMD simulation. It is shown in Figure 5(b) that α_M on the portion of the surface that has almost no contaminant is the same as that on the clean surface ($\alpha_{M,0}$) and α_M is close to zero in the region that is fully covered by the organic contaminants. In the two edge regions of the contaminants, the water surface is partially covered by the organic contaminants, as shown in Figure 1(b), and the surface coverage of the contaminants changes gradually from 100% to 0%. Moreover, the position of the organic contaminants has random fluctuations on the water surface at thermal equilibrium. Hence, it is reasonable to see in Figure 5(b) that α_M in the two edge regions of the contaminants gradually varies from near zero to $\alpha_{M,0}$. Based on the above observation, we assume $\alpha_M = \alpha_{M,0}$ in the surface region that is not covered by the organic contaminants and $\alpha_M = 0$ in the surface region that is covered by the organic contaminants. Accordingly, α_M on a contaminated water surface has a linear dependence on the contaminant sc,

$$\alpha_M = \alpha_{M,0}(1 - \text{sc}) \tag{9}$$

To corroborate the prediction of α_M from eq 9, we gradually change the sc of contaminants from 0 to 98% and determine α_M for each case. Since we placed a liquid eicosane semicylinder on the water surface at the beginning of the simulation, the x−y projection of the eicosane contaminants on the water surface after equilibration exhibits a stripe shape for cases with 42%, 54%, and 66% sc as shown in the insets of Figure 6(a). In the case of 25% sc, the stripe width is too thin

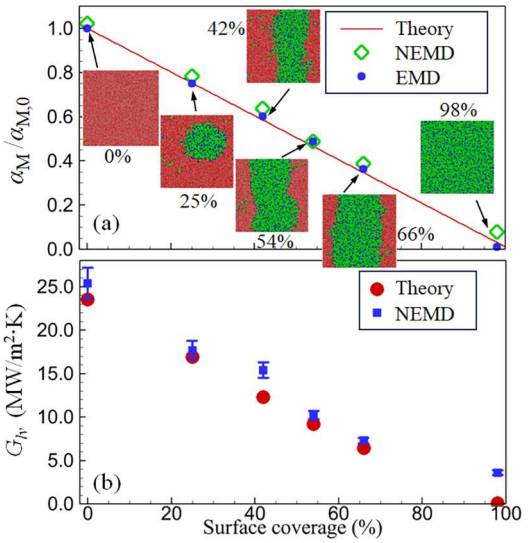

Figure 6. (a) The ratio of the MAC on a contaminated water surface to the MAC on a clean water surface as a function of surface coverage of organic contaminants. The theoretical prediction is from eq 9. The uncertainty of the MAC obtained from MD simulations in (a) is less than the symbol size. The insets in (a) are the top view of snapshots of contaminated surfaces with different surface coverage. (b) The liquid−vapor interfacial thermal resistance (G_{lv}) at the condensing liquid surface as a function of surface coverage. The theoretical prediction of G_{lv} is from eq 11.

and it breaks up and shrinks into a circular shape. Figure 6(a) shows that α_M determined from the EMD simulation agrees with the eq 9 prediction very well. In the next section, we will further investigate if the NEMD simulation predicts the same α_M value as the EMD simulation.

4.3. NEMD Determination of MAC. In NEMD simulations, we determine the temperatures (T_L, T_v) and densities ($\rho_g(T_L)$, ρ_v) of water near the liquid−vapor interface, the molar flux (J), and the macroscopic velocity ($v_{v,0}$) of water vapor during the quasi-steady-state evaporation and condensation process, and we plug them into the Schrage equation (eq 2) to calculate α_M. Figure 2 shows the NEMD simulation results for the representative simulation case with a 54% surface coverage of organic contaminants on the model water

https://doi.org/10.1021/acs.jpcb.3c06939
J. Phys. Chem. B 2024, 128, 585−595

surface. As shown in Figure 2(b), the temperatures at the evaporating liquid−vapor interface and condensing liquid−vapor interface are $T_{L,1}$ = 427.1 K and $T_{L,2}$ = 398.5 K, respectively. Accordingly, we obtain $\rho_g(T_{L,1})$ = 0.130 mol/L and $\rho_g(T_{L,2})$ = 0.057 mol/L from the ρ_g vs T data found in our previous work.[27] It is shown in Figures 2(b) and 2(c) that the temperature (T_v = 420 K) and density (ρ_v = 0.108 mol/L) of water vapor are essentially constant in the gas region, indicating that the heat and mass transfer in the vapor phase is dominated by convection, rather than diffusive processes. In addition, we obtain the molar flux of water vapor as J = 0.52 ± 0.01 mol/cm^2·s from the NEMD simulation and the vapor macroscopic velocity as $v_{v,0}$ = 48 m/s from the relation $J = \rho_v v_{x,0}$. Substituting these NEMD simulation results into the Schrage equation, we obtain α_M = 0.80 ± 0.02 on the left clean water surface and α_M = 0.43 ± 0.01 on the right contaminated water surface, which are in excellent agreement with the EMD simulation results $\alpha_{M,0}(T_{L,1})$ = 0.80 (obtained from Figure 4) and α_M = 0.43 ± 0.01 (obtained in Section 4.2).

The NEMD simulation results imply that the Schrage equation is still accurate in the prediction of the condensation rate on a contaminated water surface. To provide a better understanding of this result, we evenly divide the NEMD model system into 20 bins in the y direction and calculate the molar flux distribution at x = 15 nm (i.e., near the evaporating clean water surface) and at x = 185 nm (i.e., near the condensing contaminated water surface) as shown in Figures 7(a) and 7(b). Near the clean water surface, we observe that the local molar flux is essentially all in the x direction and has a uniform distribution as expected. When the organic contaminants are present on the water surface, Figure 7(b) shows the molar flux distribution near the contaminated surface is perturbed and the water vapor flows preferably to surface regions that are not covered by organic contaminants. However, such a small perturbation of the molar flux is not consequential to the velocity distribution (VD) of water vapor molecules near the condensing water surface. As shown in Figure 7(c), the VDs measured near the clean water surface and contaminated water surface in the NEMD model both closely follow (coefficient of determination R^2 > 0.9996) the shifted Maxwell velocity distribution (SMVD) predicted by eq 3. This means that the key assumption of the molecular VD in the derivation of the Schrage equation is still valid near a contaminated water surface. Hence, it is reasonable to see that the NEMD prediction of the MAC, which is based on the Schrage equation, is consistent with the EMD prediction for the contaminated water surface.

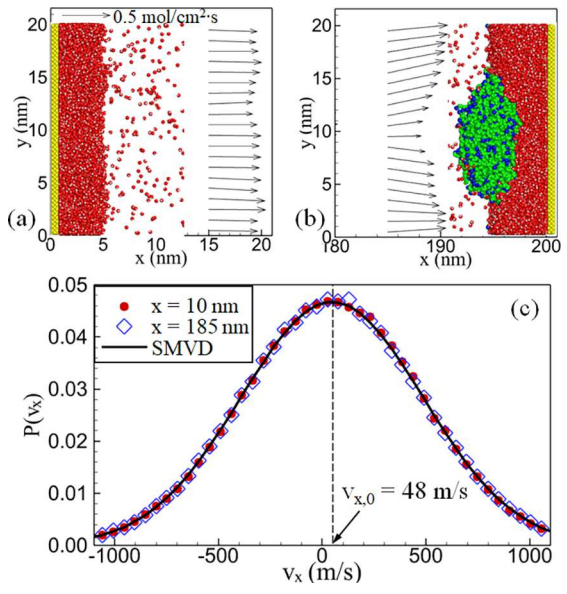

Figure 7. Y-direction distribution of the molar flux of water vapor at (a) x = 15 nm (i.e., near the evaporating surface) and at (b) x = 185 nm (i.e., near the condensing surface) in the model system shown in Figure 2. The top arrow in (a) represents the molar flux scale of 0.5 mol/cm^2·s. (c) The velocity distribution of water vapor molecules at x = 15 nm (first bin in the gas region) and x = 185 nm (last bin in the gas region), respectively, determined from the NEMD simulation and the theoretical prediction from the shifted Maxwell velocity distribution.

It is shown in Table 1 and Figure 6(a) that the NEMD predictions of α_M agree with the EMD predictions very well in all cases except for Case #6 where the EMD simulation predicts that α_M on the water surface that is almost fully covered by the organic contaminants is only ∼0.01, but the NEMD simulation predicts a much higher α_M (∼0.07). We believe the reason for the discrepancy between EMD and NEMD predictions of α_M is that we used the molar flux in the vapor phase as the condensation flux, J, at the contaminated water surface. When a vapor molecule is incident on a contaminated surface, however, it can be adsorbed by the organic surface in addition to being accommodated by liquid water. The EMD simulation only considers accommodation of vapor molecules by liquid water. Once the water surface is fully covered by an organic layer, incident water vapor molecules must be first adsorbed by the organic layer and then diffuse through the nanoscopic organic layer before they are accommodated by the liquid water. The EMD prediction of α_M = 0.01 ± 0.01 indicates that the possibility of water condensation through this channel is very low. When the water surface is covered by a 3.5 nm-thick organic layer as shown in Figure 8, we find from the NEMD simulation that there is almost no change in the amount of liquid water behind the organic layer during the 2 ns quasi-steady-state condensation process. If we use the rate of liquid water volume change to determine the condensation flux J in the NEMD simulation, we obtain $J \approx 0$ and accordingly $\alpha_M \approx 0$, which is consistent with the EMD prediction. Since water condensation is suppressed by the organic layer, an evident temperature gradient in the gas region is observed in Figure 8(b), indicating that heat conduction starts to play a role in energy transport through the gas region.

As shown in Figures 2(a) and 8(a), there are only a few eicosane molecules in the vapor phase due to the very low (below 10^{-4} mol/L) saturated vapor density of eicosane. When an eicosane vapor molecule is occasionally emitted from the contaminated water surface, it travels to the left and collides with water vapor molecules along the way. The collisions between the individual eicosane molecule and water vapor molecules cause a perturbation in the velocity and temperature of water vapor near the eicosane molecule, which increases the uncertainty in the local vapor temperature. The relatively large temperature uncertainties in the center-right portion of Figure 8 indicate that, during the 2 ns data collection period of the NEMD simulation, the number of emitted eicosane molecules in this region, the time when these eicosane molecules were emitted, and the distance these eicosane molecules travel vary significantly among different independent runs.

https://doi.org/10.1021/acs.jpcb.3c06939
J. Phys. Chem. B 2024, 128, 585−595

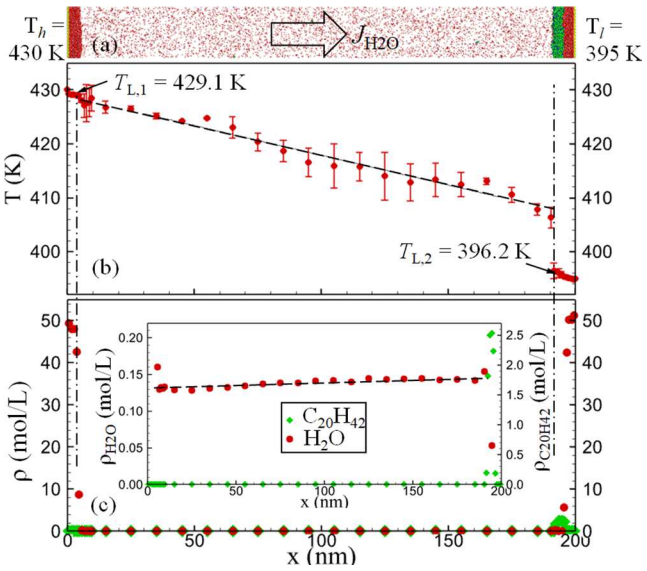

Figure 8. (a) A snapshot of the model system during NEMD simulation with T_h = 430 K, T_l = 395 K, and 98% surface coverage of organic contaminant on the condensing liquid surface. Steady-state (b) temperature, and (c) density profiles in the model system. The inset in (c) shows the density profile in the gas region. The dashed lines in (b) and (c) show the linear fit to the temperature and density distribution in the gas region, respectively. The vertical dash-dot lines indicate the location of the liquid water surfaces.

4.4. The Adsorption of Water Molecules on the Organic Surface. While the full coverage of the water surface by organic contaminants suppresses water condensation, it creates more organic surface area to adsorb water vapor molecules. Under the nonequilibrium conditions shown in Figure 8, a molar flux $J = 0.12 \pm 0.02$ mol/cm^2·s is obtained in the vapor phase during quasi-steady-state condensation/adsorption. To verify that the vapor flow is mainly caused by adsorption of water vapor molecules on the organic surface, we monitor the time variation of water density in three neighboring bins near the interface between the organic layer and water vapor. The total width of three bins is 3 nm, and the rightmost bin is located at the position where the eicosane density is nearly half of the liquid eicosane density. It is shown in Figure 9 that the average water density in the three bins near the organic surface increases almost linearly with time at a speed of 0.34 mol/(L·ns). Accordingly, water adsorption flux at the eicosane surface is ~0.10 mol/cm^2·s, which is close to J = 0.12 ± 0.02 mol/cm^2·s obtained in the vapor phase. Since the vapor molar flux in this case is dominated by the adsorption flux, using the vapor molar flux as the condensation flux, J, in the Schrage equation overestimates α_M, i.e., the fraction of incident vapor molecules that are accommodated by the liquid water.

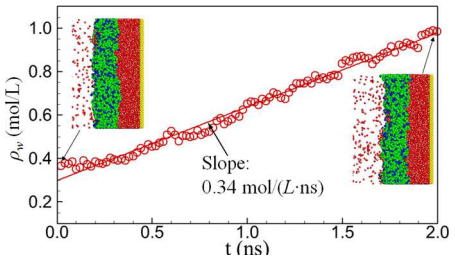

Figure 9. Density of water in the liquid−gas interface of the organic surface in Figure 8 during the 2 ns quasi-steady-state condensation/adsorption process. The straight line is the linear fit to the water density vs time data obtained from the NEMD simulation. The left and right insets are the snapshots near the organic surface at the beginning and end of the 2 ns condensation/adsorption process.

The insets of Figure 9 show that water molecules and small water clusters are adsorbed on the organic surface and a liquid waterlike overlayer has not formed yet. This confirms that it is a nonequilibrium water adsorption process rather than a condensation process. The water adsorption process is strongly affected by water−eicosane interactions and the organic surface roughness, while the water condensation process is, in contrast, dominated by water−water interactions.[62,63] Therefore, the Schrage equation, which is accurate in the prediction of water condensation rate, cannot be simply applied to predict the nonequilibrium water adsorption rate on the organic surface.[63] For other simulation cases in this work, the water surface is only partially covered by the organic contaminants, and the water condensation flux dominates over the adsorption flux. In these cases, it is valid to use the vapor molar flux in the Schrage equation to predict α_M, and the EMD and NEMD simulations predict consistent α_M values.

Figure 6(a) and Table 1 show that α_M determined from NEMD is slightly higher than that determined from EMD for most of the simulation cases. There are two reasons leading to the small discrepancies between the NEMD and EMD predictions of α_M. First, the Schrage equation, i.e., eq 2, assumes an isotropic temperature of vapor near an evaporating/condensing surface. However, our recent studies show the temperature anisotropy of vapor near an evaporating/condensing surface, and it is more accurate to use the vapor temperature normal to the liquid−vapor interface in the Schrage equation to predict the evaporation/condensation rate.[64,65] Second, when the water surface is partially covered by the organic contaminants, there is a small contribution from the adsorption flux to the total vapor molar flux near the condensing surface. Accordingly, the vapor molar flux obtained directly from the NEMD simulation slightly overestimates the condensing flux, which leads to a slightly overpredicted α_M value from the NEMD method.

4.5. Effects of Surface Contamination on Interfacial Thermal Conductance. The MD simulation results show that the Schrage equation is still valid in the prediction of the condensation rate on a water surface partially covered by organic contaminants. In this section, we use the Schrage equation for a further study of interfacial thermal conductance at the contaminated water surface. The liquid−vapor interfacial thermal conductance is defined as

$$G_{lv} = q/\Delta T \tag{10}$$

where q is the heat flux across the liquid−vapor interface and ΔT is the temperature jump across the interface. In NEMD simulations, q across the condensing liquid−vapor interface can be directly determined from the heat flux removed from the cold Au plate during the quasi-steady state, and ΔT between liquid and vapor at the interface can be obtained from the liquid and gas phase temperature profiles such as those shown in Figures 2(b) and 8(b). Hence, we can readily predict G_{lv} from NEMD simulation results and use this direct NEMD prediction to verify the theoretical prediction of G_{lv} from the Schrage equation. It is shown in our previous work[18] that

https://doi.org/10.1021/acs.jpcb.3c06939
J. Phys. Chem. B 2024, 128, 585−595

assuming $\Delta T/T_L \ll 1$, $\rho_v = \rho_g(T_v)$, and water vapor is an ideal gas, the Schrage equation gives

$$G_{lv} = h_{fg}(T_L)\frac{2\alpha_M(T_L)}{2-\alpha_M(T_L)}\sqrt{\frac{R}{2\pi M\overline{T}_{lv}}}\rho_g(\overline{T}_{lv})\left(\frac{h_{fg}(\overline{T}_{lv})}{R\overline{T}_{lv}}-\frac{1}{2}\right) \quad (11)$$

where $\overline{T}_{lv} = (T_L + T_v)/2$ at the interface and h_{fg} is the latent heat of vaporization of the model water. Since the condensation on the contaminated water surface in our MD model occurs at ~400 K, we use $h_{fg}(T = 400\ \text{K}) = 41$ kJ/mol obtained from our previous work[27] in eq 11 to predict G_{lv}. In addition, for each simulation case we use α_M determined from the EMD simulation in eq 11 to predict G_{lv} and find the theoretical prediction based on the Schrage equation has a reasonable agreement with the NEMD prediction as shown in Figure 6(b). Equation 11 predicts that G_{lv} decreases with decreasing α_M. For the representative case with a contaminant sc of 54% on the condensing surface shown in Figure 2, $\alpha_M = 0.80$ on the clean evaporating water surface is much higher than $\alpha_M = 0.43$ on the contaminated condensing surface. As a result, the G_{lv} on the left clean water surface is much greater than that on the right contaminated water surface. A greater G_{lv} leads to a smaller temperature jump ΔT across the liquid−vapor interface for a given heat flux. Hence, it is reasonable to see in Figure 2 that ΔT across the clean liquid−vapor interface is significantly smaller than that across the contaminated liquid−vapor interface.

In the case of the water surface fully covered by the organic layer, we show in Section 4.4 that the water adsorption process dominates over the water condensation process, and the Schrage equation becomes invalid. Accordingly, eq 11, which is derived from the Schrage equation, also becomes invalid for the prediction of G_{lv}. Only when the water layer adsorbed on the organic surface is thick enough to be considered as a bulk liquid such as that shown in Figure 3, the α_M value will return to $\alpha_{M,0}$ (i.e., the MAC on a clean water surface), and eq 2 and eq 11 will be valid again for the prediction of condensation rate and interfacial thermal conductance.

5. CONCLUSIONS

Both EMD and NEMD simulations are carried out to study the effects of organic surface contamination, which is immiscible with water, on the MAC of water. The MD simulation results show that the MAC on a contaminated water surface decreases almost linearly with an increase in surface coverage of the organic contaminants. On a contaminated water surface, both water condensation on the water surface and water adsorption on the organic surface can occur. The NEMD simulation results indicate that the Schrage equation is still accurate in the prediction of the MAC at a contaminated water surface if the water condensation rate dominates over the water adsorption rate. In this case, the theoretical equation (i.e., eq 11) derived from the Schrage equation gives a good prediction of the interfacial thermal conductance at the contaminated water surface. When the water surface is almost fully covered by a nanoscopic organic layer, the water adsorption process dominates over the water condensation process. In this case, the Schrage equation cannot be used to predict the water adsorption rate unless the thin water film adsorbed on the organic surface becomes thick enough to be considered as bulk liquid water.

All of the analysis in this work is based on MD simulation results in a model fluid mixture of water and eicosane at a temperature around 400 K. While we expect that the results are general, it is imperative in the future to also investigate if the conclusions drawn in this work can be applied to systems with other fluid combinations and at different temperatures.

■ ASSOCIATED CONTENT

Supporting Information

The Supporting Information is available free of charge at https://pubs.acs.org/doi/10.1021/acs.jpcb.3c06939.

Determination of the contact angle and the surface coverage of the organic contaminants on the model water surface (PDF)

■ AUTHOR INFORMATION

Corresponding Author

Zhi Liang − *Department of Mechanical and Aerospace Engineering, Missouri University of Science and Technology, Rolla, Missouri 65409, United States;* orcid.org/0000-0002-2173-2951; Phone: 573-341-4982; Email: zlch5@mst.edu

Authors

Jordan Hartfield − *Department of Mechanical and Aerospace Engineering, Missouri University of Science and Technology, Rolla, Missouri 65409, United States*

Eric Bird − *Department of Mechanical and Aerospace Engineering, Missouri University of Science and Technology, Rolla, Missouri 65409, United States;* orcid.org/0009-0002-3051-577X

Complete contact information is available at: https://pubs.acs.org/10.1021/acs.jpcb.3c06939

Notes

The authors declare no competing financial interest.

■ ACKNOWLEDGMENTS

This work was supported by NSF under Grant No. 2310833. Additionally, we would like to thank the Advanced Cyberinfrastructure Coordination Ecosystem: Service and Support (ACCESS) for providing us supercomputer resources for MD simulations.

■ REFERENCES

(1) Kakitsuba, N. Dynamic Changes in Sweat Rates and Evaporation Rates through Clothing during Hot Exposure. *J. Therm. Biol.* **2004**, *29*, 739−742.

(2) Fu, M.; Yu, T.; Zhang, H.; Arens, E.; Weng, W.; Yuan, H. A Model of Heat and Moisture Transfer through Clothing Integrated with the UC Berkeley Comfort Model. *Build. Environ.* **2014**, *80*, 96−104.

(3) Denmead, O.; Dunin, F.; Leuning, R.; Raupach, M. Measuring and Modelling Soil Evaporation in Wheat Crops. *Phys. Chem. Earth* **1996**, *21* (3), 97−100.

(4) Loaiciga, H. A.; Valdes, J. B.; Vogel, R.; Garvey, J.; Schwarz, H. Global Warming and the Hydrologic Cycle. *J. Hydrol.* **1996**, *174*, 83−127.

(5) Lu, Z.; Salamon, T. R.; Narayanan, S.; Bagnall, K. R.; Hanks, D. F.; Antao, D. S.; Barabadi, B.; Sircar, J.; Simon, M. E.; Wang, E. N. Design and Modeling of Membrane-Based Evaporative Cooling Devices for Thermal Management of High Heat Fluxes. *IEEE Trans. Compon. Packag. Technol.* **2016**, *6*, 1056−1065.

(6) Humplik, T.; Lee, J.; O'Hern, S.; Fellman, B.; Baig, M.; Hassan, S.; Atieh, M.; Rahman, F.; Laoui, T.; Karnik, R. Nanostructured materials for water desalination. *Nanotechnology* **2011**, *22*, 292001.
(7) Sefiane, K. On the Formation of Regular Patterns from Drying Droplets and Their Potential Use for Bio-Medical Applications. *J. Bionic Eng.* **2010**, *7*, S82−S93.
(8) Persad, A. H.; Ward, C. A. Expressions for the evaporation and condensation in the Hertz-Knudsen relation. *Chem. Rev.* **2016**, *116*, 7727.
(9) Hertz, H. Ueber die Verdunstung der Flüssigkeiten, insbesondere des Quecksilbers, im luftleeren Raume. *Ann. Phys.* **1882**, *253*, 177.
(10) Knudsen, M. *Kinetic Theory of Gases*, 3rd ed.; Methuen: London, 1950.
(11) Schrage, R. W. *A Theoretical Study of Interphase Mass Transfer*; Columbia University Press: New York, 1953.
(12) Carey, V. P. *Liquid−Vapor Phase-Change Phenomena*; Hemisphere, Publishing House: New York, 1992.
(13) Persad, A. H.; Ward, C. A. Expressions for the Evaporation and Condensation Coefficients in the Hertz-Knudsen Relation. *Chem. Rev.* **2016**, *116*, 7727.
(14) Cheng, S.; Lechman, J. B.; Plimpton, S. J.; Grest, G. S. Evaporation of Lennard-Jones fluids. *J. Chem. Phys.* **2011**, *134*, 224704.
(15) Meland, R.; Frezzotti, A.; Ytrehus, T.; Hafskjold, B. Nonequilibrium molecular-dynamics simulation of net evaporation and net condensation, and evaluation of the gas-kinetic boundary condition at the interphase. *Phys. Fluids* **2004**, *16*, 223.
(16) Tabe, H.; Kobayashi, K.; Fujii, H.; Watanabe, M. Molecular dynamics simulation of evaporation coefficient of vapor molecules during steady net evaporation in binary mixture system. *Int. J. Heat Mass Transfer* **2022**, *188*, 122663.
(17) Liang, Z.; Keblinski, P. Molecular simulation of steady-state evaporation and condensation in the presence of a non-condensable gas. *J. Chem. Phys.* **2018**, *148*, No. 064708.
(18) Liang, Z.; Biben, T.; Keblinski, P. Molecular simulation of steady-state evaporation and condensation: validity of the Schrage relationships. *Int. J. Heat Mass Transfer* **2017**, *114*, 105.
(19) Gonzalez, J.; Ortega, J.; Liang, Z. Prediction of thermal conductance at liquid-gas interfaces using molecular dynamics simulations. *Int. J. Heat Mass Transfer* **2018**, *126*, 1183.
(20) Cao, B.-Y.; Xie, J.-F.; Sazhin, S. S. Molecular dynamics study on evaporation and condensation of n-dodecane at liquid-vapor phase equilibria. *J. Chem. Phys.* **2011**, *134*, 164309.
(21) Xie, J.-F.; Sazhin, S. S.; Cao, B.-Y. Molecular dynamics study of the processes in the vicinity of the n-dodecane vapour/liquid interface. *Phys. Fluids* **2011**, *23*, 112104.
(22) Nagayama, G.; Takematsu, M.; Tsuruta, T. Condensation/evaporation coefficient of chain molecules. *Trans. Jpn. Soc. Mech. Eng.* **2013**, *79*, 2149.
(23) Nagayama, G.; Takematsu, M.; Mizuguchi, H.; Tsuruta, T. Molecular dynamics study on condensation/evaporation coefficients of chain molecules at liquid−vapor interface. *J. Chem. Phys.* **2015**, *143*, No. 014706.
(24) Bird, E.; Gutierrez Plascencia, J.; Liang, Z. Thermal transport across the interface between liquid n-dodecane and its own vapor: A molecular dynamics study. *J. Chem. Phys.* **2020**, *152*, 184701.
(25) Chandra, A.; Keblinski, P. Investigating the validity of Schrage relationships for water using molecular dynamics simulations. *J. Chem. Phys.* **2020**, *153*, 124505.
(26) Tsuruta, T.; Nagayama, G. Molecular dynamics studies on the condensation coefficient of water. *J. Phys. Chem. B* **2004**, *108*, 1736.
(27) Bird, E.; Gutierrez Plascencia, J.; Keblinski, P.; Liang, Z. Molecular simulation of steady-state evaporation and condensation of water in air. *Int. J. Heat Mass Transfer* **2022**, *184*, 122285.
(28) Julin, J.; Shiraiwa, M.; Miles, R. E. H.; Reid, J. P.; Pöschl, U.; Riipinen, I. Mass accommodation of Water: Bridging the Gap Between Molecular Dynamics Simulations and Kinetic Condensation Models. *J. Phys. Chem. A* **2013**, *117*, 410.
(29) Morita, A.; Sugiyama, M.; Kameda, H.; Koda, S.; Hanson, D. R. Mass Accommodation Coefficient of Water: Molecular Dynamics Simulation and Revised Analysis of Droplet Train/Flow Reactor Experiment. *J. Phys. Chem. B* **2004**, *108*, 9111.
(30) Barclay, P. L.; Lukes, J. R. Curvature Dependence of the Mass Accommodation Coefficient. *Langmuir* **2019**, *35*, 6196.
(31) Katzenstein, A. S.; Doezema, L. A.; Simpson, I. J.; Blake, D. R.; Rowland, F. S. Extensive regional atmospheric hydrocarbon pollution in the southwestern United States. *PNAS 100* **2003**, *100*, 11975.
(32) Illing, C. J.; Hallmann, C.; Miller b, K. E.; Summons b, R. E.; Strauss, H. Airborne hydrocarbon contamination from laboratory atmospheres. *Organic Geochemistry 76* **2014**, *76*, 26.
(33) Guo, W.; Chen, B.; Do, V. L.; ten Brink, G. H.; Kooi, B. J.; Svetovoy, V. B.; Palasantzas, G. Effect of Airborne Hydrocarbons on the Wettability of Phase Change Nanoparticle Decorated Surfaces. *ACS Nano* **2019**, *13*, 13430.
(34) Song, Y.; Preston, D. J.; Zhang, L.; Wang, E. N. Effect of Contaminant Adsorption on Critical Heat Flux during Pool Boiling, The Second Pacific Rim Thermal Engineering Conference, PRTEC-24305, Maui, Hawaii, USA.
(35) Javadi, A.; Moradi, N.; Mohwald, H.; Miller, R. Adsorption of alkanes from the vapour phase on water drops measured by drop profile analysis tensiometry. *Soft Matter* **2010**, *6*, 4710.
(36) Kairaliyeva, T.; Fainerman, V. B.; Aksenenko, E. V.; Kovalchuk, V. I.; Tarasevich, Yu. I.; Miller, R. Adsorption of alkane vapor at water drop surfaces. *Colloids Surf., A* **2017**, *532*, 541.
(37) Marek, R.; Straub, J. Analysis of the Evaporation Coefficient and the Condensation Coefficient of Water. *Int. J. Heat Mass Transfer* **2001**, *44*, 39.
(38) Pound, G.; Selected, M. Values of Evaporation and Condensation Coefficients for Simple Substances. *J. Phys. Chem. Ref. Data* **1972**, *1*, 135.
(39) Lu, Z.; Kinefuchi, I.; Wilke, K. L.; Vaartstra, G.; Wang, E. N. A unified relationship for evaporation kinetics at low Mach numbers. *Nat. Commun.* **2019**, *10*, 2368.
(40) Liang, Z.; Chandra, A.; Bird, E.; Keblinski, P. A molecular dynamics study of transient evaporation and condensation. *Int. J. Heat Mass Transfer* **2020**, *149*, 119152.
(41) Berendsen, H. J. C.; Grigera, J. R.; Straatsma, T. P. The Missing Term in Effective Pair Potentials. *J. Phys. Chem.* **1987**, *91*, 6269.
(42) Wolf, D.; Keblinski, P.; Phillpot, S. R.; Eggebrecht, J. Exact Method for the Simulation of Coulombic Systems by Spherically Truncated, Pairwise r-1 Summation. *J. Chem. Phys.* **1999**, *110*, 8254.
(43) Mendoza, F. N.; López-Lemus, J.; Chapela, G. A.; Alejandre, J. The Wolf Method Applied to the Liquid-Vapor Interface of Water. *J. Chem. Phys.* **2008**, *129*, No. 024706.
(44) Nath, S. K.; Escobedo, F. A.; de Pablo, J. J. On the simulation of vapor−liquid equilibria for alkanes. *J. Chem. Phys.* **1998**, *108*, 9905.
(45) Khare, R.; de Pablo, J. J.; Yethiraj, A. Rheological, thermodynamic, and structural studies of linear and branched alkanes under shear. *J. Chem. Phys.* **1997**, *107*, 6956.
(46) Pine, S. H. *Organic Chemistry*, 2nd ed.; McGraw-Hill: New York, 1964.
(47) van der Ploeg, P.; Berendsen, H. J. C. Molecular dynamics simulation of a bilayer membrane. *J. Chem. Phys.* **1982**, *76*, 3271.
(48) Jorgensen, W. L.; Madura, J. D.; Swenson, C. J. Optimized intermolecular potential functions for liquid hydrocarbons. *J. Am. Chem. Soc.* **1984**, *106*, 6638.
(49) Smit, B.; Karaborni, S.; Siepmann, J. I. Computer simulations of vapour liquid phase equilibria of n-alkanes. *J. Chem. Phys.* **1995**, *102*, 2126.
(50) Frenkel, D.; Smit, B. *Understanding Molecular Simulation*; Springer: Berlin, 2002.
(51) Foiles, S. M.; Baskes, M. I.; Daw, M. S. Embedded-atom-method functions for the fcc metals Cu, Ag, Au, Ni, Pd, Pt, and their alloys. *Phys. Rev. B* **1986**, *33*, 7983.
(52) Rappe, A. K.; Casewit, C. J.; Colwell, K. S.; Goddard, W. A.; Skiff, W. M. UFF, a full periodic table force field for molecular

https://doi.org/10.1021/acs.jpcb.3c06939
J. Phys. Chem. B 2024, 128, 585−595

mechanics and molecular dynamics simulations. *J. Am. Chem. Soc.* **1992**, *114*, 10024.
(53) Rowlinson, J. S.; Widom, B. *Molecular Theory of Capillarity*; Dover Publications, Inc.: Mineola, NY, 2002 (for spreading coefficient and contact angle).
(54) Neupane, P.; Wilemski, G. Molecular dynamics study of wetting of alkanes on water: from high temperature to the supercooled region and the influence of second inflection points of interfacial tensions. *Phys. Chem. Chem. Phys.* **2021**, *23*, 14465.
(55) Allen, M. P.; Tildesley, D. J. *Computer Simulation of Liquids*; Clarendon Press: Oxford, U.K., 2000.
(56) Omelyan, I. P. Algorithm for numerical integration of the rigid-body equations of motion. *Phys. Rev. E* **1998**, *58*, 1169.
(57) Berendsen, H. J. C.; Postma, J. P. M.; Van Gunsteren, W. F.; Di Nola, A.; Haak, J. R. Molecular dynamics with coupling to an external bath. *J. Chem. Phys.* **1984**, *81*, 3684.
(58) Lemmon, E. W.; Bell, I. H.; Huber, M. L.; McLinden, M. O. Thermophysical Properties of Fluid Systems. In *NIST Chemistry WebBook*, NIST Standard Reference Database Number 69; Linstrom, P. J., Mallard, W. G., Eds.; National Institute of Standards and Technology: Gaithersburg, MD. DOI: 10.18434/T4D303 (retrieved October 6, 2023).
(59) Müller, E. A.; Mejía, A. Comparison of United-Atom Potentials for the Simulation of Vapor-Liquid Equilibria and interfacial Properties of Long-Chain n-Alkanes up to n-C100. *J. Phys. Chem. B* **2011**, *115*, 12822.
(60) Kirkwood, J. G.; Buff, F. P. The statistical mechanical theory of surface tension. *J. Chem. Phys.* **1949**, *17*, 338.
(61) Walton, J. P.; Tildesley, D. J.; Rowlinson, J. S.; Henderson, J. R. The pressure tensor at the planar surface of a liquid. *Mol. Phys.* **1983**, *48*, 1357.
(62) Yesilbas, M.; Boily, J.-F. Particle size controls on water adsorption and condensation regimes at mineral surfaces. *Sci. Reports* **2016**, *6*, 32136.
(63) Yaghoubian, S.; Zandavi, S. H.; Ward, C. A. From adsorption to condensation: the role of adsorbed molecular clusters. *Phys. Chem. Chem. Phys.* **2016**, *18*, 21481.
(64) Bird, E.; Liang, Z. Transport phenomena in the Knudsen layer near an evaporating surface. *Phys. Rev. E* **2019**, *100*, No. 043108.
(65) Bird, E.; Liang, Z. Maximum evaporation flux of molecular fluids from a planar liquid surface. *Phys. Rev. E* **2020**, *102*, No. 043102.